Chemical Science

ROYAL SOCIETY OF CHEMISTRY

EDGE ARTICLE

View Article Online
View Journal

Cite this: DOI: 10.1039/d6sc00562d

All publication charges for this article have been paid for by the Royal Society of Chemistry

Radical-to-radical push–pull effect enhances single-molecule conductance in asymmetric diradicals

Dacheng Dai,[a] Qian Zhan,[a] Tianfang Shi,[a] Xiaodong Liu, *[a] Lichuan Chen,[b] Sergio Moles Quintero, [c] Dongsheng Wang, *[a] Juan Casado *[c] and Yonghao Zheng *[ad]

Asymmetry produces a unique modulation of diradical character through the appearance of a push–pull electron spin effect when the two unpaired electrons reside in radical moieties of different electron donor (benzo-1,3-dithiol-2-ylidene)/acceptor (phenoxyl) character. Herein, asymmetric diradical substructures are perpendicularly appended to a linear bisphenyl-thiophene segment whose thiomethyl ends are linked to metal electrodes. Using a scanning tunneling microscope break junction technique, we measured the conductance of these diradicals. In the non-radical parents, the whole conductance is investigated through the linear conjugation path between the thiomethyls. In the diradicals, conductance increases compared to that of their non-radical parents, which is taken as fine-tuning by the presence of unpaired electrons of the primordial linear-path conductance. From a molecular orbital perspective, such enhancement is due to the inclusion of new intragap states (*i.e.*, near the Fermi energy level). From a valence bond perspective, the increase is due to the additional linear conjugation channel provided by the hypervalent state of sulfur resulting from bonding of the two unpaired electrons by a push–pull electron spin effect. Also, there is a reduction of the conductance by enlarging the donor–acceptor moiety with more phenyl groups as a result of the variable weights of the hypervalent sulfur form and of the zwitterionic form. Therefore, the single-molecule junction technique can allow the establishment of relationships between intramolecular radical–radical coupling in off-site diradicals and single-molecule conductance tuning.

Received 20th January 2026
Accepted 1st April 2026

DOI: 10.1039/d6sc00562d

rsc.li/chemical-science

Introduction

The advance in the field of single molecule electronics towards the realization of competitive devices requires the existence of molecules with diverse electronic inputs able to multiply the functionality in devices.[1–4] In this way, for a given molecular transmission path, the capacity of fine tuning the overall molecular conductance (*i.e.*, even from turning it on and off) by means of consistent and progressive molecular/chemical substitution is very welcome.[5,6] An appealing strategy that we have been developing for the last few years is the use of pairs of unpaired electrons (*i.e.*, diradicals) as elements of conductance tuning.[7] In comparison to closed-shell systems, the existence of diradical molecules provokes different scenarios: (i) the opening of new circuits of molecular conductance through the appearance of radical–radical bonding, (ii) the labile nature of unpaired electrons also provides an opportunity for the incorporation of electron transfer events, (iii) the intrinsic spin of the radicals also produces the sum of magnetic effects on conductance, *etc.* The exploration of the interconnection between the electronic properties of individual organic molecules with unpaired electrons and conductance is crucial when these act as electrical active wires.[8,9]

The immense majority of diradical molecules have symmetric structures,[10–14] while asymmetric diradicals represent a subclass that has been little studied and remains a largely uncharted territory as conducting elements in single-molecule conductance devices. Asymmetry produces a unique modulation of diradical character through the appearance of a push–pull electron spin effect when the two unpaired electrons reside in moieties of different electron donor/acceptor nature (*i.e.*, see Scheme 1 where one electron of one SOMO delocalizes over the other SOMO with lower energy overall resulting in one spin pairing over to the other). This effect is analogous to the well-

[a]*School of Optoelectronic Science and Engineering, University of Electronic Science and Technology of China (UESTC), Chengdu 611731, People's Republic of China. E-mail: zhengyonghao@uestc.edu.cn; xdliu@uestc.edu.cn; wangds@uestc.edu.cn*

[b]*Institute of Modern Optics and Center of Single-Molecule Science, Tianjin Key Laboratory of Micro-Scale Optical Information Science and Technology, Nankai University, Tianjin 300350, People's Republic of China*

[c]*Department of Physical Chemistry, University of Málaga, Campus de Teatinos s/n, Málaga 29071, Spain. E-mail: casado@uma.es*

[d]*State Key Laboratory of Physical Chemistry of Solid Surfaces, Xiamen University, Xiamen 361005, People's Republic of China*

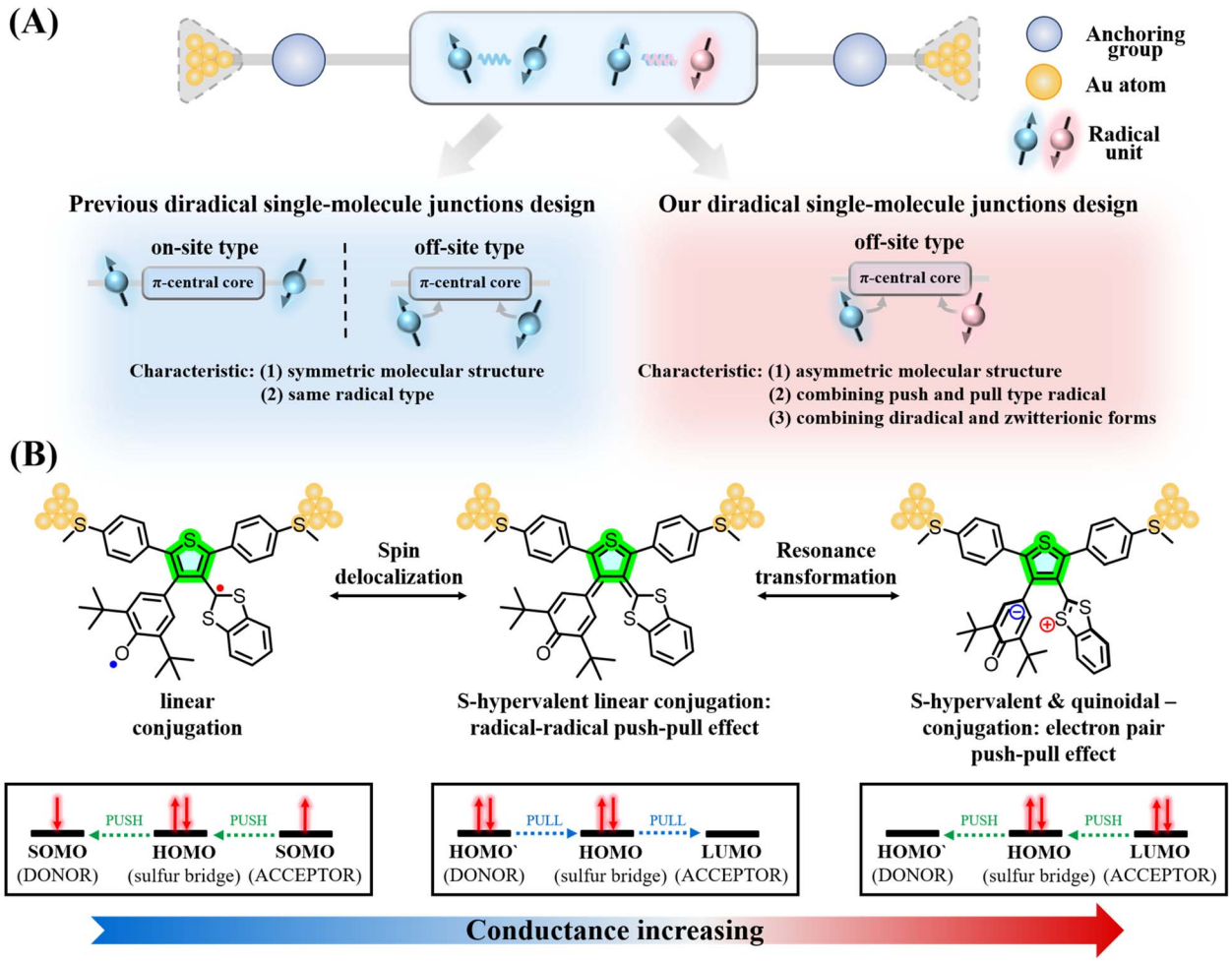

Scheme 1 (A) Schematic of diradical based single-molecule junctions. The past design and the novel design strategies of diradical single-molecule junctions presented in this paper. (B) Schematic of the evolution of thiophene derivatives in molecular junctions.

known push–pull (two) electron effect typically found in push–pull donor–acceptor molecules.[15,16]

Two main strategies exist for the inclusion of two unpaired electrons in molecules for single molecular conductance, on-site and off-site modalities, depending on whether the radicals are placed "on" or "off" relative to the main conductance channel (Scheme 1A) which is usually the linear conjugation path between the electrode anchoring groups.[7,17–22] Many studies have revealed how unpaired electrons in symmetric diradicals interact with conduction electrons injected in the molecules from the electrodes at the single-molecule level.[23–25] The most pronounced changes (orders of magnitude) in conductance are imparted by symmetric diradicals placed "on-site" of the conduction channel whereas "off-site" symmetric diradicals play the role of fine tuning/gating the overall conductance output. Now, we want to address the single molecular conductance actuation of "off-site" asymmetric diradicals. The synthesis of asymmetric diradicals is complex. Indeed, only very few reports of asymmetric diradical-based single-molecule junctions are available, all based on the "on-site" modality.

In this work, we designed and synthesized three asymmetric diradicals, named **Di-T1R**, **Di-T2R** and **Di-T3R**, based on a bis-phenyl-thiophene central core (thus possessing the same conductance path and molecular junction lengths). Specifically, the methyl sulfide (–SMe) anchoring groups are attached to the phenylenes,[26,27] whereas one phenoxy radical (acceptor-type) and one benzo-1,3-dithiol-2-ylidene radical (donor-type) are attached to the thiophene ring at the 3,4-positions (Scheme 1B).[28,29] Using a scanning tunneling microscope break junction (STM-BJ) technique,[30,31] we successfully constructed, for the first time, asymmetric diradical-based single-molecule junctions and analyzed the impact of the intramolecular push–pull spin effect on off-site asymmetric diradicals in the tuning of single-molecule conductance. Our single-molecule measurements reveal that the conductance values of **Di-T1R**, **Di-T2R** and **Di-T3R** ($10^{-3.64}G_0$, $10^{-3.88}G_0$ and $10^{-3.79}G_0$, respectively) increase compared to that of their non-radical counterparts **Di-T1**, **Di-T2** and **Di-T3** ($10^{-4.14}G_0$, $10^{-4.19}G_0$ and $10^{-4.15}G_0$, respectively), and among the three diradicals, **Di-T1R** exhibits the largest conductance. Our primary objective is to disentangle new molecular and electronic properties in light of the conductance measurements. The strong perturbation of the electronic structure in the molecular junction under the application of a strong electric bias can reveal unique emerging properties which can help to design new diradicals with enhanced properties.

Results and discussion

Synthesis

The synthetic method of the asymmetric diradical molecules primarily includes the following three major steps, which enables us to rapidly and efficiently obtain the target products[32–37] (Fig. 1 and Section S2): (1) the introduction of phenylmethylthio (–PhSMe) groups at the 2,5-positions of the thiophene core through palladium-catalyzed Suzuki–Miyaura cross-coupling; (2) the introduction of a phenoxy ring and benzo-1,3-dithiol-2-ylidene at the 3,4-positions of the thiophene core; (3) the oxidation of the non-radical molecules with lead dioxide. All the molecules possess the same conduction pathway, with –SMe groups as the Au tip anchoring units.

Analysis of the electronic structure

The spin and electron density distributions of the three asymmetric diradicals exhibit different shapes as shown in Fig. S1. First, for the diradical **Di-T1R**, the electron distributions on the side of the dithiol radical is significantly higher than those on the side of the phenoxy radical in line with the asymmetric electronic structure setting up the conditions for a push–pull spin/radical effect over the "off-site" substitution path. It is worth describing the relevant valence bonds, and Lewis or resonance forms of these asymmetric diradicals (see Scheme 2A for **Di-T1R** as an example), which are valid for a qualitative and intuitive understanding of the phenomena but do not intend to be quantitative descriptors. The resonance form **a** places the two radicals outside the linear conjugation path between the two thiomethyl groups and hence resembles that of the non-radical parents. By delocalizing the radicals over the central thiophene, several possibilities appear: (i) resonance form **b** locates the two radicals at the 2,5 thiophene positions, producing a situation of conjugation blockade by cross-conjugation of the off-site groups; (ii) resonance form **c** stablishes a bonding coupling between the radicals over a hypervalent sulfur which opens a new linear conjugated delocalization path from the thiomethyl groups (*i.e.*, avoiding the cross-conjugation path) through the sulfur atom; and (iii) resonance form **d** derives from form **c** and represents a conventional donor–acceptor coupling, giving rise to

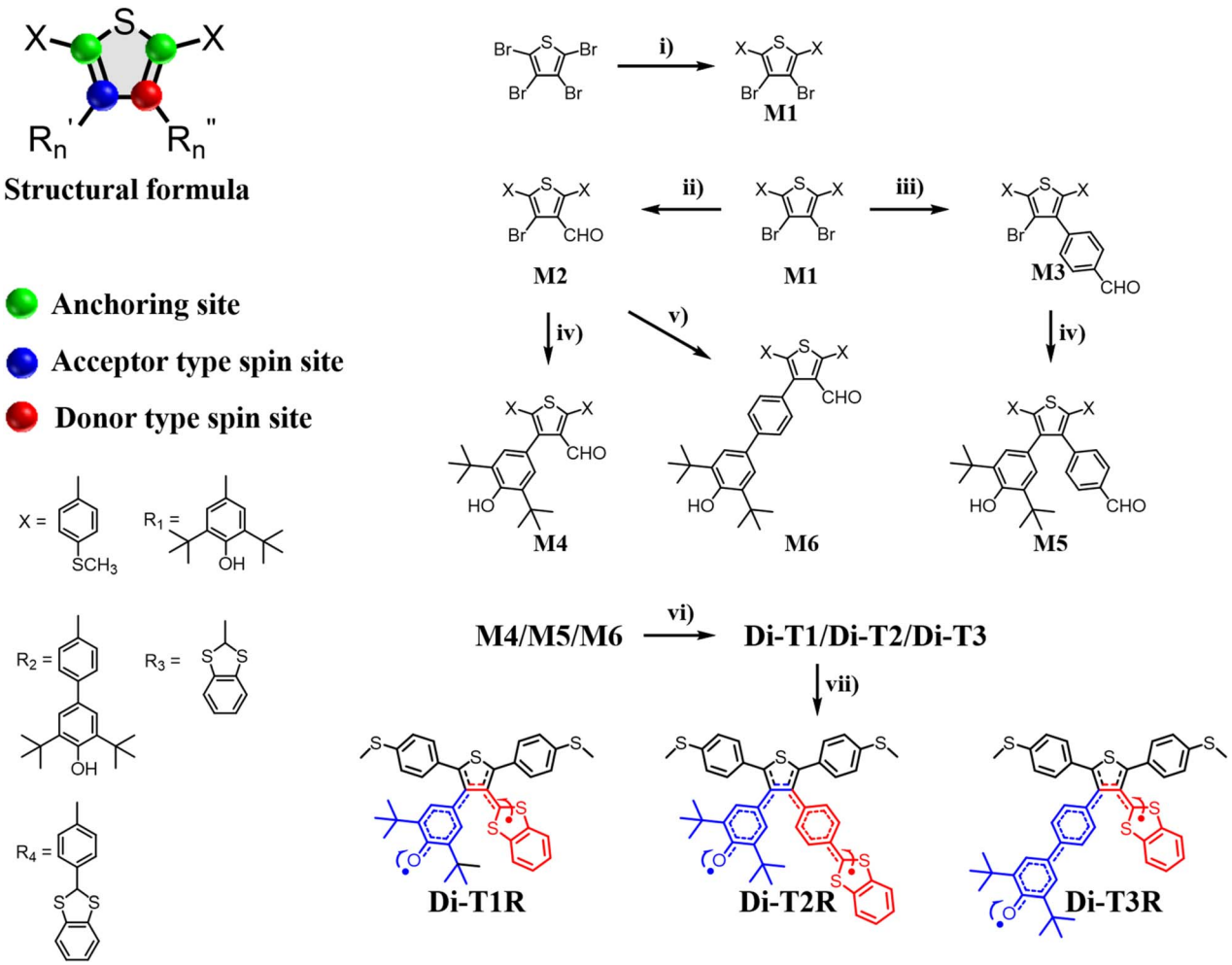

Fig. 1 The structural formula and synthetic route of asymmetric diradicals. Reagents and conditions: (i) $Pd(PPh_3)_2Cl_2$, K_2CO_3, 4-(methylthio) phenylboronic acid, DMF, EtOH, 65 °C; (ii) *n*-BuLi, DMF, −78 °C; (iii) Cs_2CO_3, $Pd(dppf)Cl_2$, THF, H_2O, 70 °C; (iv) phenol group, $Pd(dppf)Cl_2$, Cs_2CO_3, THF, H_2O, 70 °C; (v) phenol group, Cs_2CO_3, THF, $Pd(dppf)Cl_2$, H_2O, 70 °C; (vi) 1,2-benzenedithiol, *p*-TSOH, toluene, 105 °C; (vii) PbO_2, DCM, RT.

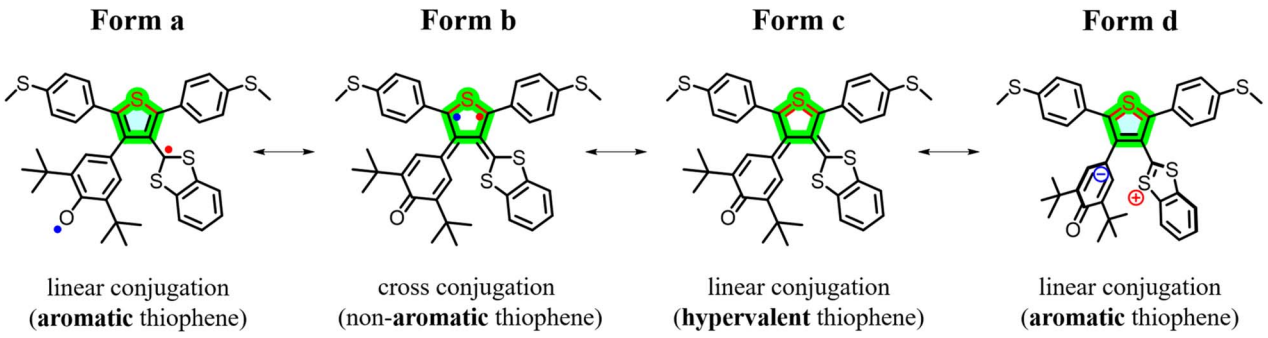

Scheme 2 Lewis and electronic resonance forms of Di-T1R.

a zwitterionic form (*i.e.*, by moving pairs of electrons) which has the additional property of removing cross-conjugation from the central thiophene.

The degree of radical delocalization (Fig. S1) over the main linear conjugated sequence follows the order **Di-T1R** > **Di-T3R** > **Di-T2R**. The inclusion of more benzene bridges on the asymmetric moieties leads to the lowering of the efficiency of the formation of the closed-shell forms **c** and **d** as show in Scheme 2A given that these are formed at the cost of the breaking of benzene aromaticity in the diradical state (Scheme 2B). In order to support this resonance form discussion, NICS values have been calculated for the studied compounds (Fig. S2). From these NICS data we infer that (i) in the diradical states the aromatic character of the central thiophene rings decreases as a result of radical delocalization over this ring; and (ii) the less negative NICS value is found for **Di-T1R** indicating the larger reduction of aromatic character upon inclusion of the radicals, in line (see below) with the larger weight of the S-hypervalent form.

Absorption and EPR spectroscopies and electrochemical properties

The ultraviolet (UV)-visible (vis)-near infrared (NIR) absorption spectra of the non-radical molecules **Di-T1**, **Di-T2**, and **Di-T3** show almost no absorption peaks in the visible region, with their main absorption features located in the UV region (Fig. S3). In contrast, the UV-visible-NIR absorption spectra of the asymmetric diradicals **Di-T1R**, **Di-T2R**, and **Di-T3R** exhibit different degrees of redshift. **Di-T1R** and **Di-T3R** show a single absorption peak in the visible region at 618 and 549 nm, respectively, while the diradical **Di-T2R** displays two absorption peaks in the visible region at 645 and 430 nm. Clearly, the occurrence of longer wavelength absorptions in the diradical molecules indicates the presence of intragap states from which optical excitations at longer wavelengths can take place.

The electrostatic potential distribution maps of the three asymmetric diradicals (Fig. S4) and in particular **Di-T1R** displays neat segregation of the negative/positive charge in the phenoxyl/dithiol groups, a partial zwitterionic form that produces solvatochromism in solvents of different polarities as displayed in Fig. 2A. With increasing solvent polarity, the absorption peak exhibits a pronounced redshift, progressing from 610 nm (CCl_4) to 622 nm (2-MeTHF), then to 627 nm (DCM), and finally to 639 nm (DMF). As shown in Fig. 2A, the comparison reveals that the degree of red shift is in the order of **Di-T1R** > **Di-T3R** > **Di-T2R**.

The formation of radicals was further confirmed by the electron spin resonance (ESR) spectra (Fig. 2B). We investigated the magnetic behaviors of **Di-T1R**, **Di-T2R**, and **Di-T3R** in the solid state by measuring their variable-temperature magnetic susceptibility using ESR in the temperature range of 140–290 K. The singlet–triplet energy gap (ΔE_{S-T}) values of **Di-T1R**, **Di-T2R**, and **Di-T3R** were estimated by fitting the IT–*T* curves with the modified Bleaney–Bowers equation,[38,39] giving ΔE_{S-T} values of −2.67, −1.12, and −0.74 kcal mol^{-1} respectively (Fig. 2C), which agrees with the trend of UDFT calculated ΔE_{S-T} of −4.66, −0.14, and −0.01 kcal mol^{-1}. Note that for **Di-T2R** and **Di-T3R**, half-field forbidden transition signals ($\Delta m_s = \pm 2$) were also detected, indicating the thermal population of excited spin-triplet states (insets of Fig. 2B). According to the ΔE_{S-T} magnetic gaps, **Di-T1R** exhibits larger closed-shell contribution (smaller diradical character, y_0) in agreement with the contributions of the closed-shell singlet hypervalent and zwitterionic forms. Combining the analyses of mass spectrometry, ESR and UV-vis-NIR absorption spectra for the three diradicals, we unambiguously confirm their existence.

Cyclic voltammetry of **Di-T1R**, **Di-T2R**, and **Di-T3R** in dry dichloromethane (DCM) shows reduction waves at $E_{1/2}^{red} = -0.70$, −0.76, and −0.72 V (*versus* Fc^+/Fc, Fc = ferrocene), and oxidation waves at $E_{1/2}^{ox} = 0.27$, 0.29, and 0.31 V, respectively (Fig. S5). Accordingly, the singly occupied molecular orbital/singly unoccupied molecular orbital (SOMO/SUMO) energy levels were estimated to be −5.07/−4.10 eV, −5.09/−4.04 eV, and −5.11/−4.08 eV for **Di-T1R**, **Di-T2R**, and **Di-T3R**, respectively. The electrochemical energy gaps (E_g^{EC}) were thus calculated to be 0.97, 1.05, and 1.03 eV, respectively, which are in good accordance with their optical energy gaps (Fig. 2D).

Single molecular conductance measurements

The design strategy and STM-BJ structure are shown in Fig. 3A and B. The single-molecule conductance of all the compounds in

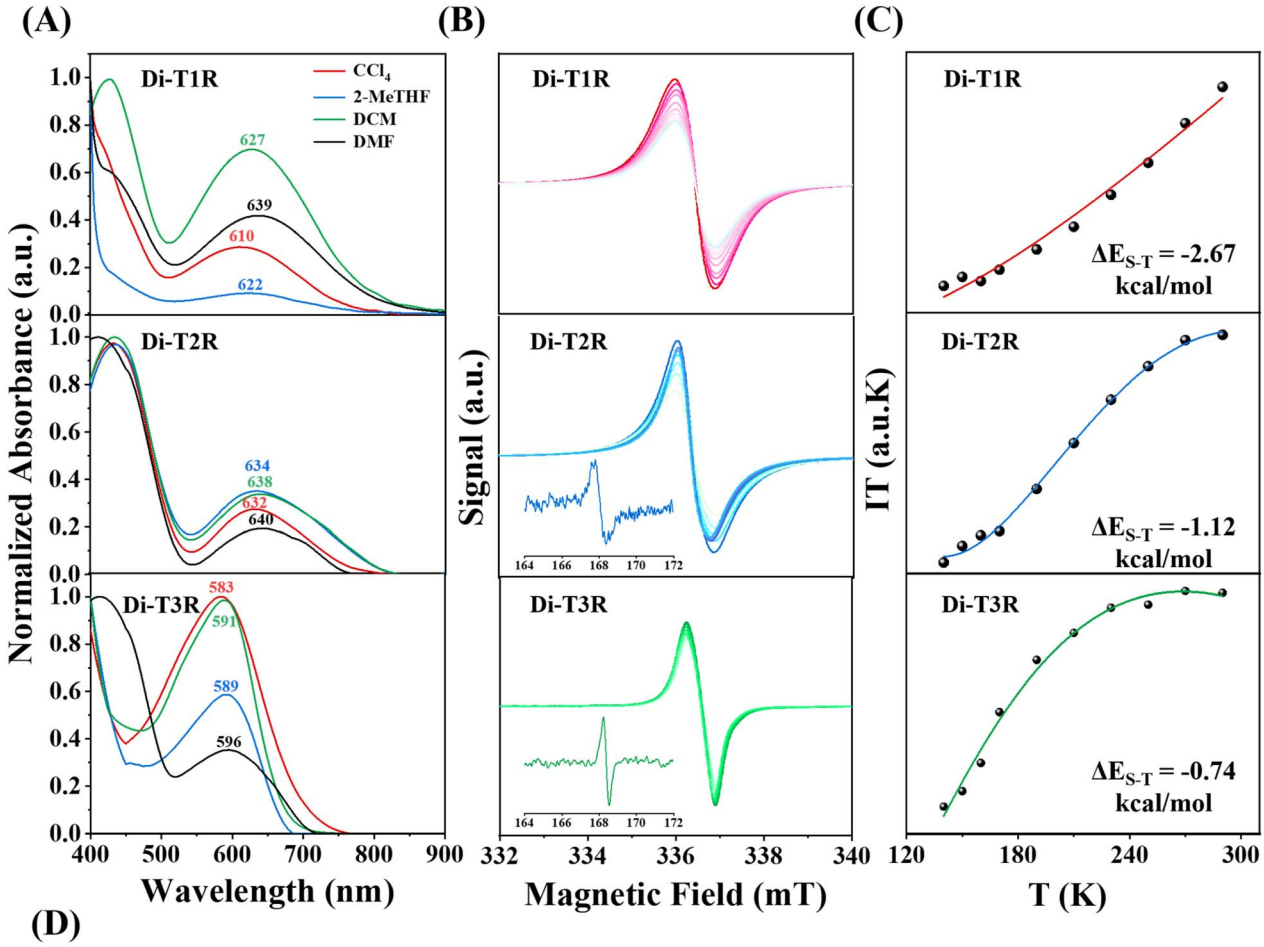

(D)

Sample	SOMO[a](eV)	SUMO[a](eV)	E_g^{EC} [b] (eV)	E_g^{Opt} [c] (eV)	Half-life[d] (hours)	$\Delta E_{S\text{-}T}$ [e] (kcal/mol)	y[f]	Conductance [g] ($\log(G/G_0)$)
Di-T1R	**-5.07**	**-4.10**	**0.97**	**1.52**	**38**	**-2.67**	**0.074**	**-3.64**
Di-T2R	**-5.09**	**-4.04**	**1.05**	**1.43**	**30**	**-1.12**	**0.74**	**-3.87**
Di-T3R	**-5.11**	**-4.08**	**1.03**	**1.67**	**23**	**-0.74**	**0.99**	**-3.79**

Fig. 2 (A) UV-vis-NIR electronic absorption spectra of **Di-T1R**, **Di-T2R**, **and Di-T3R** in solvents of different polarities (red: CCl_4, blue: 2-MeTHF, green: DCM, and dark: DMF). (B) ESR measurements of **Di-T1R**, **Di-T2R**, and **Di-T3R**. (C) The measured (black sphere) and fitted (solid line) $I \times T$–T curves of **Di-T1R**, **Di-T2R**, and **Di-T3R** based on the VT ESR measurements. (D) The summarized physical properties of the selected compounds. The [a]SOMO and SUMO were calculated from cyclic voltammetry; [b]E_g^{Ec}: electrochemical SOMO–SUMO energy gap; [c]E_g^{opt}: optical energy gap estimated from the onset of the absorption spectra; [d]the chemical stability of the radicals by monitoring the time evolution of their UV-vis-NIR absorption spectra under ambient conditions; [e]ΔE_{S-T} was estimated by fitting the $I \times T$–T curves with the Bleaney–Bowers equation; [f]calculated at the level of ub3lyp/6-31G(d) based on the occupation number of the lowest unoccupied natural orbital (LUNO); [g]single-molecule conductance measured *via* STM-BJ.

degassed 1,2,4-trichlorobenzene (TCB) solutions was measured at room temperature (RT) in air. For all the diradicals, the measurements were taken within 10 minutes after purification to ensure the accuracy of our data. Fig. 3C presents their 2D conductance-displacement histograms obtained by superimposing more than 2000 independent traces. All molecules exhibit well-defined conductance intensity clouds with different plateau heights.

Further analysis of the relative-displacement distributions of all molecular junctions reveals that the lengths of the molecular junctions are all about 1.15 nm after adding the gold–gold snap-back distance of ~0.5 nm.[40] This value is in good agreement with their theoretically (U)DFT calculated molecular lengths of ~1.40 nm, suggesting that the conductance features come from the fully stretched molecular configurations.

Fig. 3D shows the 1D conductance histograms of the di-radicals **Di-T1R**, **Di-T2R**, and **Di-T3R**, along with their corresponding **Di-T1**, **Di-T2** and **Di-T3** non-radical compounds. Through Gaussian fitting, the most probable conductance

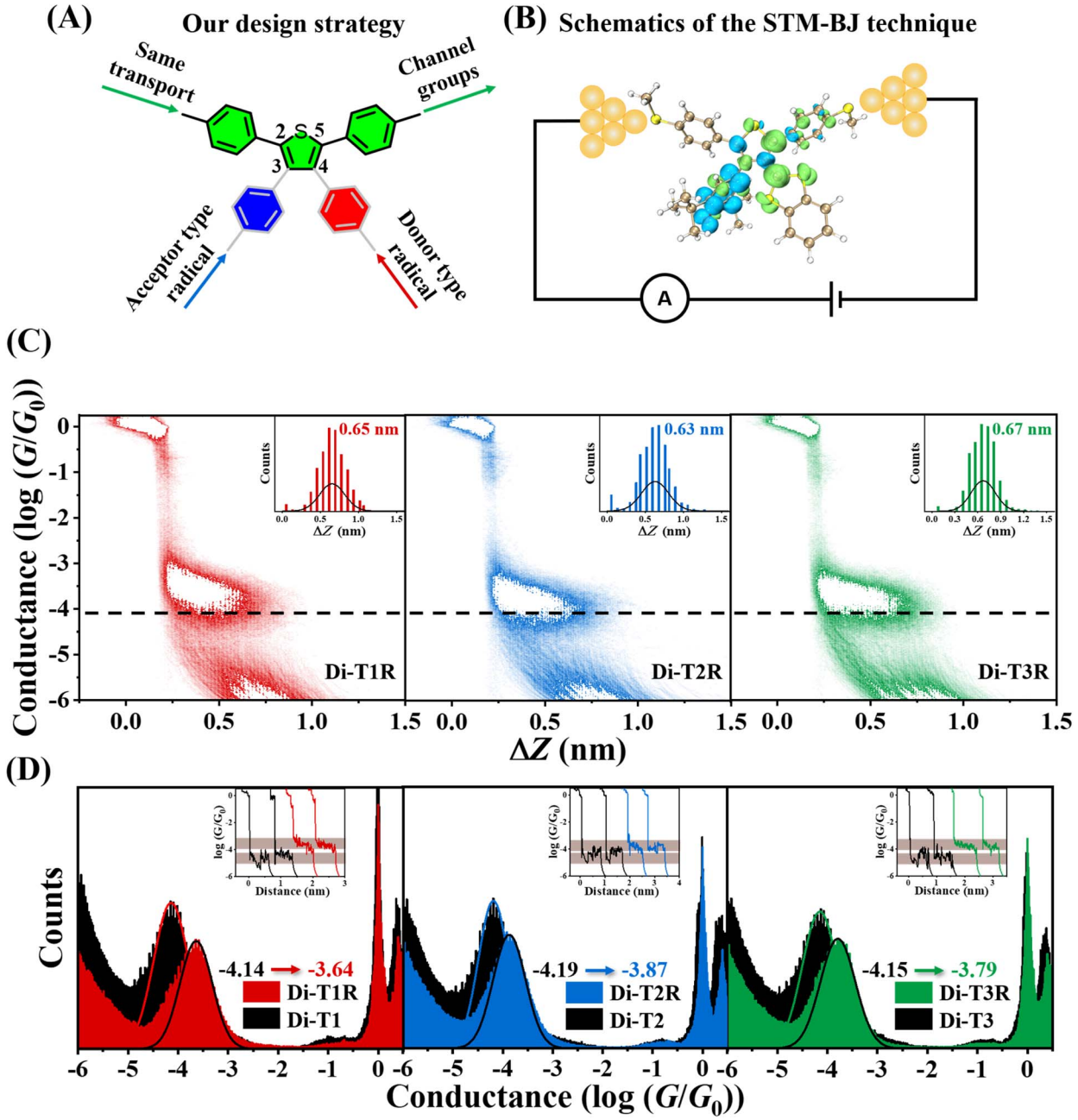

Fig. 3 Room temperature conductance measurements of asymmetric diradicals. (A) Our design strategy. (B) Schematic of the **Di-T1R** single-molecule junction. (C) The 2D conductance-displacement histograms of **Di-T1R**, **Di-T2R**, and **Di-T3R**. The insets show the relative displacement distributions. (D) The 1D conductance histograms of **Di-T1**, **Di-T2** and **Di-T2R** series molecule devices. The insets show the typical individual conductance traces.

values of **Di-T1**, **Di-T2**, and **Di-T3** are $10^{-4.14}G_0$, $10^{-4.19}G_0$ and $10^{-4.15}G_0$, respectively, which indicates that for the same conduction pathway in the non-radical molecules, introducing different types of substituents at the 3,4-positions of the thiophene ring has little or no effect on the molecular conductance. This indicates two things: (i) these G_0 values are provided by the linear conduction path between the thiomethyls; and (ii) the negligible influence of the cross-conjugated groups over the main linear conjugated path.

In comparison to the non-radical molecules (*i.e.*, with linear conjugation alone), the asymmetric diradicals **Di-T1R**, **Di-T2R** and **Di-T3R** show higher conductance values of $10^{-3.64}G_0$, $10^{-3.88}G_0$ and $10^{-3.79}G_0$, respectively (Fig. 3D). The formation of the diradical species in resonance form **b** reinforces the bonding over the 3,4-thiophene positions producing quantum destructive interference over the linear conjugated path by cross-conjugation. This conductance detracting effect is compensated/overpassed by the full pairing of the two radicals over a hypervalent form of the sulfur (resonance form **c** and **d**)

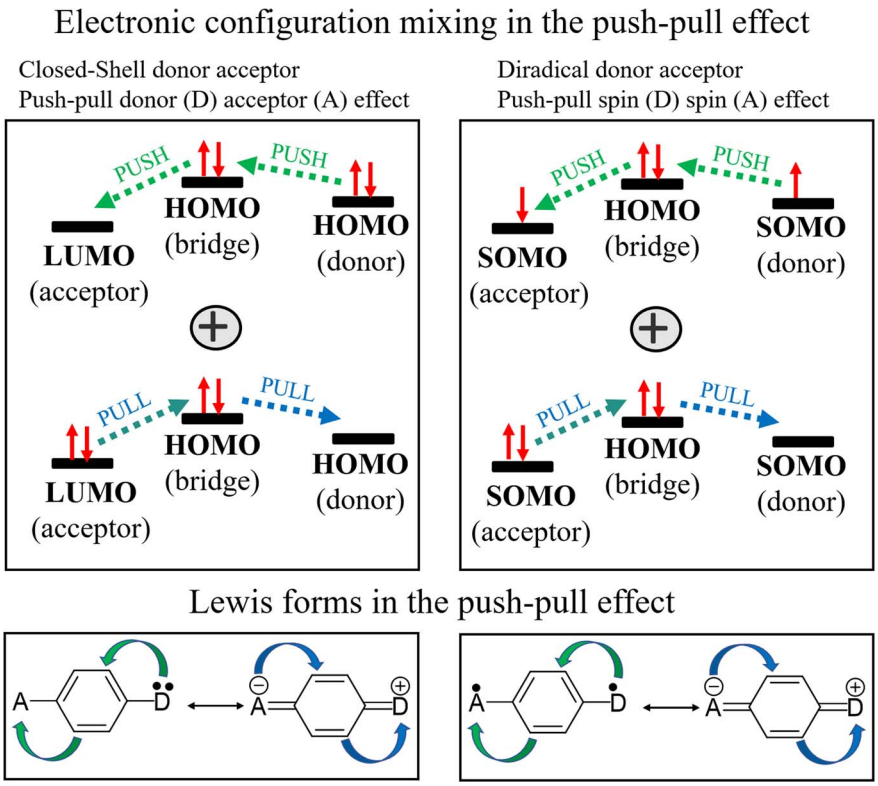

Fig. 4 Orbital and valence bond description of the push–pull spin effect in closed-shell donor-to-acceptor molecules and in open-shell donor–acceptor diradicals.

which opens an alternative linear conjugation path through the sulfur atom between the thiomethyls. In addition, from resonance form **c** a through bond donor → acceptor electron transfer can take place which weakens double bonds at the 3,4-thiophene positions in a zwitterionic state (resonance form **d**). From this valence bond analysis, the increase in conductance in the diradical (*i.e.*, *versus* the non-radicals) is carried out by forms **c** and **d**. Furthermore, the conductance of the three asymmetric diradicals exhibits a trend of **Di-T1R** > **Di-T3R** > **Di-T2R**. Given that the formation of the hypervalent sulfur channel in **Di-T1R** requires the smallest benzene aromaticity breaking of the three molecules, this enables the prominent stabilization of resonance form **c** and **d**, and subsequently the largest increase in conductance. Interestingly, the largest conductance of **Di-T1R** then correlates with the smallest diradical character (*i.e.*, largest antiferromagnetic coupling through the hypervalent sulfur) which is the opposite situation found when diradicals are included over the main linear conduction channel. The antiferromagnetic hypervalent state is brought about by the appearance of a push–pull spin effect (*i.e.*, see Fig. 4 where one electron of one SOMO delocalizes over the SOMO with lower energy overall resulting in one spin moving to the other orbital) in analogy to the effect of push–pull donor–acceptor coupling.

Single molecular conductance calculations

To further explore the effect of the molecular structure on single-molecule conductance, we used Gaussian software to calculate the molecular structure properties of the three pairs of diradical/non-radical molecules **Di-T1R**/**Di-T1**, **Di-T2R**/**Di-T2** and **Di-T3R**/**Di-T3**.[41,42] The results show that the LUMO and HOMO of closed-shell non-radical molecules are well-delocalized over the phenyl-thiophene backbone (Fig. S6) in accordance with a main linear conjugation/conduction channel alone. In contrast, the SOMO and SUMO frontier orbital distributions of **Di-T1R** (and similarly in **Di-T2R** and **Di-T3R**) become localized over the radical moieties. This is true either for the SOMO and SUMO in the open-shell singlet state, and in the SOMOs in the triplet state (Fig. S6). This means that the formation of unpaired electrons opens new intragap localized states that can assist the increment of conductance given the energy proximity to the Fermi energy level of the electrodes. Using the zeroth-order Green's equation to estimate the impact of the molecular orbital phase and coefficients on electron transport, we found that **Di-T1**, **Di-T2**, and **Di-T3** have the same phase and similar molecular orbital coefficients on the anchoring –SCH_3 group. However, after introducing radicals into the three molecules, the orbital localization causes significant differences in orbital coefficients as a result of delocalization and radical pairings.

As shown in Fig. 5A, **Di-T1R** further conducts using the hypervalent path and by means of the zwitterionic channel. The calculated transmission pathways in Fig. 5A correspond well with the resonance forms in Scheme 2. Theoretical simulations of the conductance transport properties indicate that the conductance values of non-radical precursors are very similar

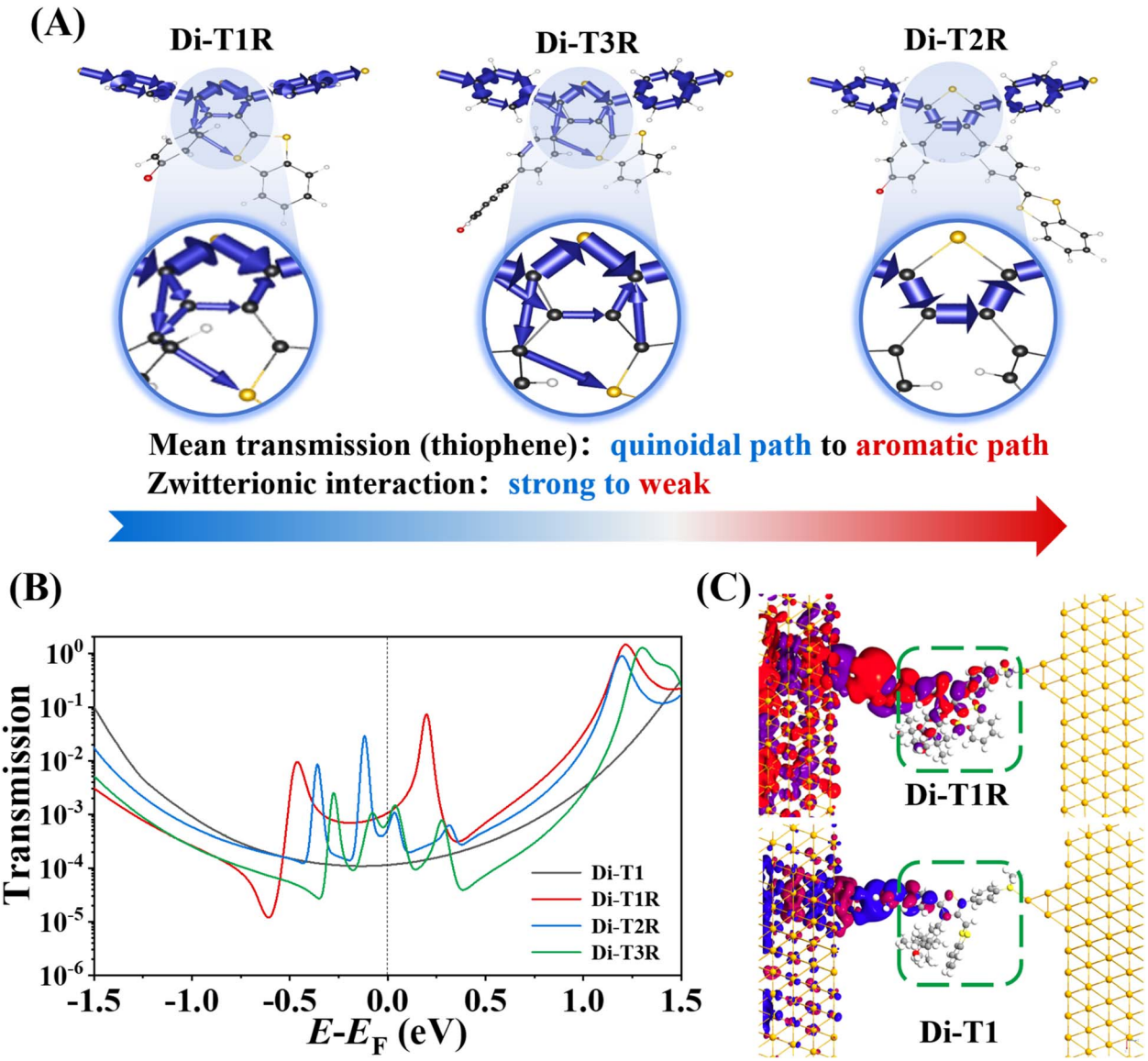

Fig. 5 Electrical transport property simulation. (A) The transmission pathways of molecular devices for **Di-T1R**, **Di-T3R**, and **Di-T2R**. (B) The calculated transmission spectra of **Di-T1**, **Di-T1R**, **Di-T2R**, and **Di-T3R** single-molecule junction. (C) The calculated transmission eigenstate for **Di-T1R** and **Di-T1** at the Fermi energy level.

for the three molecules (Fig. S7) which is consistent with the experimental measurements.[43,44] Upon diradical formation, new resonance states emerged near the Fermi level in the theoretical transmission spectra (Fig. S7) associated with the SOMO and SUMO. For instance, at the $E = E_{\mathrm{Fermi}}$ level, the theoretical conductance increases in **Di-T1** → **Di-T1R** are justified by the inclusion of intragap states (*i.e.*, the frontier orbital formed after diradical injection) (Fig. S8) which compensates for the potential cross-conjugation interference.

For **Di-T2R** and **Di-T3R**, multiple resonance peaks appeared near the Fermi level as well (Fig. 5B), also enhancing the electric transport capabilities of the diradicals compared to the non-radical molecules. A further analysis of the transmission eigenstates at the Fermi level reveals a new aspect of the devices consistent with the orbital delocalization, not only over the radical substituent groups, but also over the right electrode in the order **Di-T1R** > **Di-T3R** > **Di-T2R** (Fig. 5C and S8). It is noteworthy that the coupling strength of radical resonance peaks near the Fermi level gradually decreases when more rings are added in **Di-T2R** and **Di-T3R**.

Analysis of the transmission Hamiltonian for the molecular orbitals (LUMO and HOMO: dominant charge transport) reveals that **Di-T1R** exhibits the weakest orbital localization (Fig. S9), followed by **Di-T3R**, while **Di-T2R** shows the strongest localization, localized only to the central portion of the molecule. Therefore, we contend that free radicals not only introduce conduction pathways but also exert further impact on the molecular conformation and delocalisation through electron push–pull interactions. In this manner, they enable the regulation of molecular electronic transport properties.

It is worth mentioning that chiral-induced spin selectivity (CISS) and electric magnetochiral anisotropy (EMCA) have emerged as important mechanisms for spin-polarized electron transport in chiral molecular systems. However, the asymmetric diradicals investigated in this study (**Di-T1R**, **Di-T2R**, and **Di-T3R**) form racemic forms which preclude the manifestation of CISS or EMCA effects in these systems. Consequently, the observed conductance variations among the three diradicals can be unambiguously attributed to the differences in their intramolecular push–pull electronic effects and the relative contributions of diradical, zwitterionic/quinoid, and S-hypervalent resonance forms. Future studies on chiral analogues of these diradicals may offer valuable opportunities to explore the interplay between radical character and spin-selective electron transport.

Conclusion

In conclusion, we synthesized a series of asymmetric thiophene-based diradicals, employing phenoxy radicals as electron-acceptor units and benzo-1,3-dithiol-2-ylidene radicals as electron-donor units. ESR measurements confirmed varying degrees of radical–radical coupling driven by a push–pull electron spin effect within these asymmetric diradical molecules. We used the STM-BJ technique to measure their single-molecule conductance. All diradical molecules exhibit a conductance increase compared to their non-radical counterparts due to the appearance of intragap states close to the Fermi level that assist in conductance and that compensate for the adverse effect of cross-conjugation over the main conduction linear conjugation pathway. In valence bond terms, there appears a hypervalent sulfur state that opens an additional linear conjugation channel between the thiomethyl anchors. Among the diradical species, **Di-T1R** exhibits the strongest antiferromagnetic coupling between the unpaired electrons in the hypervalent state which further produces the conditions for the formation of a zwitterionic form by intramolecular donor–acceptor electron transfer. As a result, the location of off-site diradicals delocalizing over a linear conjugation/conduction path enables the fine tuning of the conductance. It is worth mentioning that the off-site placement of the unpaired electrons regarding the main conjugation path induces such small fine tuning of the conductance which is significantly different compared with the on-site placement of the diradical in the main conduction path which provokes an orders of magnitude increase in the conductance.

This study provides new electronic responses of molecular systems under extreme electrical perturbation conditions which, under strong electric fields, reveal intricate relationships between the molecular structure, radical spin–spin coupling, and single-molecule junction conductance.

Author contributions

Y. Z., D. W., J. C and X. L. supervised the project. D. D. carried out the synthetic work. T. S. carried out the ESR studies. D. D., Q. Z. and L. C. prepared the manuscript. S. M. Q. and J. C. contributed to the electronic structure analysis. D. D. and Q. Z. carried out the computational studies. All authors discussed the results and commented on the manuscript.

Conflicts of interest

The authors declare no competing financial interest.

Data availability

The data supporting this article have been included as part of the supplementary information (SI). Supplementary information: synthetic protocols, UV-vis spectra, theoretical computational data, and NMR spectra. See DOI: https://doi.org/10.1039/d6sc00562d.

Acknowledgements

The authors acknowledge financial support from the National Natural Science Foundation of China (22375029 and 52203134). J. C. thanks the Junta de Andalucía (PROYEXCEL-0328, P21-0328) and Ministerio de Ciencia, Innovación y Universidades of Spain (PID2024-157601NB-I00) for financial support.

Notes and references

1 P. Li, L. Zhou, C. Zhao, H. Ju, Q. Gao, W. Si, L. Cheng, J. Hao, M. Li, Y. Chen, C. Jia and X. Guo, *Rep. Prog. Phys.*, 2022, **85**, 086401.
2 S. Sanvito, *Chem. Soc. Rev.*, 2011, **40**, 3105–3118.
3 K. Yoshizawa, *Acc. Chem. Res.*, 2012, **45**, 1612–1621.
4 J. Jang and J. H. Yoon, *J. Am. Chem. Soc.*, 2024, **146**, 32206–32221.
5 L. Sun, A. Y. Diaz-Fernandez, A. T. Gschneidtner, F. Westerlund, S. Lara-Avila and K. Moth-Poulsen, *Chem. Soc. Rev.*, 2014, **43**, 7378–7411.
6 X. Liu, H. Yang, H. Harb, R. Samajdar, J. T. Woods, O. Lin, Q. Chen, A. I. B. Romo, J. Rodríguez-López, S. R. Assary, S. J. Moore and M. C. Schroeder, *Nat. Chem.*, 2024, **16**, 1772–1780.
7 H. Zhang, L. Chen, X. Liu, F. Sun, M. Zhang, M. S. Quintero, Q. Zhan, S. Jiang, J. Li, D. Wang, J. Casado, W. Hong and Y. Zheng, *Sci. Adv.*, 2024, **10**, eadp7307.
8 Y. Chelli, S. Sandhu, S. H. A. Daaoub, S. Sangtarash and H. Sadeghi, *Nano Lett.*, 2023, **23**, 3748–3753.
9 T. Gao, A. Daaoub, Z. Pan, Y. Hu, S. Yuan, Y. Li, G. Dong, R. Huang, J. Liu, S. Sangtarash, J. Shi, Y. Yang, H. Sadeghi and W. Hong, *J. Am. Chem. Soc.*, 2023, **145**, 17232–17241.
10 Z. Chen, Y. Li and F. Huang, *Chem*, 2021, **7**, 288–332.
11 Z. Zeng, X. Shi, C. Chi, T. L. J. Navarrete, J. Casado and J. Wu, *Chem. Soc. Rev.*, 2015, **44**, 6578–6596.
12 D. Yuan, W. Liu and X. Zhu, *Chem*, 2021, **7**, 333–357.
13 Z. Sun, Q. Ye, C. Chi and J. Wu, *Chem. Soc. Rev.*, 2012, **41**, 7857–7889.
14 L. Ji, J. Shi, J. Wei, T. Yu and W. Huang, *Adv. Mater.*, 2020, **32**, 1908015.

15 P. Li, W. Xiong, J. Wang, J. Hao, M. Li, B. Wang, Y. Chen, W. Si, H. Ren, G. Li, Y. Chen, J. Lv, H. Zhang, C. Jia and X. Guo, *Adv. Mater.*, 2023, **35**, 2301876.
16 Z. Chen, W. Li, A. M. Sabuj, Y. Li, W. Zhu, M. Zeng, S. C. Sarap, M. M. Huda, X. Qiao, D. Ma, Y. Ma, N. Rai and F. Huang, *Nat. Commun.*, 2021, **12**, 5889.
17 C. Yang, Z. Chen, C. Yu, J. Cao, G. Ke, W. Zhu, W. Liang, J. Huang, W. Cai, C. Saha, A. M. Sabuj, N. Rai, X. Li, J. Yang, Y. Li, F. Huang and X. Guo, *Nat. Nanotechnol.*, 2024, **19**, 978–985.
18 L. Li, Z. J. Low, J. Wilhelm, G. Liao, S. Gunasekaran, R. C. Prindle, R. L. Starr, D. Golze, C. Nuckolls, L. M. Steigerwald, F. Evers, M. L. Campos, X. Yin and L. Venkataraman, *Nat. Chem.*, 2022, **14**, 1061–1067.
19 Y. T. Baum, S. Fernández, D. Peña and S. J. H. van der Zant, *Nano Lett.*, 2022, **22**, 8086–8092.
20 B. Lawson, E. Vidal, S. Luna, M. M. Haley and M. Kamenetska, *ACS Nano*, 2024, **18**, 29059–29066.
21 R. Casares, S. Rodríguez-González, Á. Martínez-Pinel, R. I. Márquez, M. T. González, C. Díaz, F. Martín, M. J. Cuerva, E. Leary and A. Millán, *J. Am. Chem. Soc.*, 2024, **146**, 29977–29986.
22 A. Sil, L. Hamilton, M. F. J. Morris, H. S. A. Daaoub, H. H. J. Burrows, M. C. Robertson, K. Luzyanin, J. S. Higgins, H. Sadeghi, J. N. Nichols, S. Sangtarash and A. Vezzoli, *Angew. Chem., Int. Ed.*, 2024, **63**, e202410304.
23 Q. Zou, J. Qiu, Y. Zang, H. Tian and L. Venkataraman, *eScience*, 2023, **3**, 100115.
24 L. Li, R. C. Prindle, W. Shi, C. Nuckolls and L. Venkataraman, *J. Am. Chem. Soc.*, 2023, **145**, 18182–18204.
25 Y. Zhang, R. Qiu, K. Qu, C. Zhang, F. J. Stoddart and H. Chen, *Sci. China Mater.*, 2024, **67**, 709–728.
26 E. Leary, L. A. Rosa, T. M. González, G. Rubio-Bollinger, N. Agraït and N. Martín, *Chem. Soc. Rev.*, 2015, **44**, 920–942.
27 J. Hurtado-Gallego, S. Sangtarash, R. Davidson, L. Rincón-García, A. Daaoub, G. Rubio-Bollinger, J. C. Lambert, S. V. Oganesyan, R. M. Bryce, N. Agraït and H. Sadeghi, *Nano Lett.*, 2022, **22**, 948–953.
28 W. V. Manner, F. T. Markle, H. J. Freudenthal, P. J. Roth and M. J. Mayer, *Chem. Commun.*, 2008, 256–258.
29 Z. Zeng, S. Lee, M. Son, K. Fukuda, M. P. Burrezo, X. Zhu, Q. Qi, R. Li, T. L. J. Navarrete, J. Ding, J. Casado, M. Nakano, D. Kim and J. Wu, *J. Am. Chem. Soc.*, 2015, **137**, 8572–8583.
30 Y. Zheng, P. Duan, Y. Zhou, C. Li, D. Zhou, Y. Wang, L. Chen, Z. Zhu, X. Li, J. Bai, K. Qu, T. Gao, J. Shi, J. Liu, Q. C. Zhang, Z. N. Chen and W. Hong, *Angew. Chem., Int. Ed.*, 2022, **61**, e202210097.
31 J. Liu, X. Zhao, Q. Al-Galiby, X. Huang, J. Zheng, R. Li, C. Huang, Y. Yang, J. Shi, Z. D. Manrique, J. C. Lambert, R. M. Bryce and W. Hong, *Angew. Chem., Int. Ed.*, 2017, **56**, 13061–13065.
32 H. Wu, H. Hanayama, M. Coehlo, Y. Gu, Z. Wu, S. Takebayashi, G. Jakob, S. Vasylevskyi, D. Schollmeyer, M. Kläui, G. Pieters, M. Baumgarten, K. Mullen, A. Narita and Z. Qiu, *J. Am. Chem. Soc.*, 2024, **146**, 7480–7486.
33 D. Lungerich, O. Papaianina, M. Feofanov, J. Liu, M. Devarajulu, I. S. Troyanov, S. Maier and K. Amsharov, *Nat. Commun.*, 2018, **9**, 4756.
34 M. Kawaura, T. Aizawa, S. Takahashi, H. Miyasaka, H. Sotome and S. Yagai, *Chem. Sci.*, 2022, **13**, 1281–1287.
35 C. K. Nicolaou, G. P. Bulger and D. Sarlah, *Angew. Chem., Int. Ed.*, 2005, **44**, 4442–4489.
36 B. Wei, D. Zhang, Y. Chen, A. Lei and P. Knochel, *Angew. Chem., Int. Ed.*, 2019, **58**, 15631–15635.
37 K. Okano, K. Sunahara, Y. Yamane, Y. Hayashi and A. Mori, *Chem.–Eur. J.*, 2016, **22**, 16450–16454.
38 S. Mori, M. S. Quintero, N. Tabaka, R. Kishi, G. R. Núñez, A. Harbuzaru, P. R. Ortiz, J. Marín-Beloqui, S. Suzuki, C. Kitamura, J. C. Gómez-García, Y. Dai, F. Negri, M. Nakano, S. Kato and J. Casado, *Angew. Chem., Int. Ed.*, 2022, **61**, e202206680.
39 X. Xu, S. Takebayashi, H. Hanayama, S. Vasylevskyi, T. Onishi, T. Ohto, H. Tada and A. Narita, *J. Am. Chem. Soc.*, 2023, **145**, 3891–3896.
40 B. Zeng, Y. Zou, G. Wang, W. Hong, Z. Tian and Y. Yang, *Nano Today*, 2022, **47**, 101660.
41 M. P. Burrezo, W. Zeng, M. Moos, M. Holzapfel, S. Canola, F. Negri, C. Rovira, J. Veciana, H. Phan, J. Wu, C. Lambert and J. Casado, *Angew. Chem., Int. Ed.*, 2019, **58**, 14467–14471.
42 F. Miao, Y. Ji, B. Han, M. S. Quintero, H. Chen, G. Xue, L. Cai, J. Casado and Y. Zheng, *Chem. Sci.*, 2023, **14**, 2698–2705.
43 E. H. Skipper, B. Lawson, X. Pan, V. Degtiareva and M. Kamenetska, *ACS Nano*, 2023, **17**, 16107–16114.
44 M. Zhang, J. Lin, K. Song, K. Chang, X. Dai, Y. Zang and D. Zhu, *J. Am. Chem. Soc.*, 2023, **145**, 6480–6485.